Nano Energy 65 (2019) 104045

Contents lists available at ScienceDirect

Nano Energy

journal homepage: www.elsevier.com/locate/nanoen

Full paper

Converting eggs to flexible, all-solid supercapacitors

Yunya Zhang, Jiajun He, Zan Gao, Xiaodong Li*

Department of Mechanical and Aerospace Engineering, University of Virginia, 122 Engineer's Way, Charlottesville, VA, 22904-4746, USA

ARTICLE INFO

Keywords:
Egg
Biomass
Graphene
Supercapacitor
All-solid
Flexible

ABSTRACT

The rapid expansion of electrochemical energy storage market has imposed an impending need for low-cost, sustainable materials for high-performance electrodes, separators, and electrolytes. A rational strategy is to derive the electrochemical materials from renewable biomass. However, how to comprehensively and effectively utilize biomass remains challenging. Here, we report flexible, all-solid supercapacitors constructed with the materials entirely from eggs. Eggshells and white/yolk were used to produce 2D graphene-like carbon for constructing electrodes while egg white/yolk, on the other hand, was found to be a gel-like solid-state electrolyte with competitive ionic conductivity. With eggshell membrane as a superb separator, flexible, all-solid supercapacitors were assembled which exhibited superlative electrochemical performance and mechanical flexibility. The prototypical study inspires a smart approach to comprehensively and effectively use biomass materials for constructing energy storage devices. The eggshell-enabled graphene-like carbon and protein-derived solid-state electrolyte should find extensive applications in various fields.

1. Introduction

Continued development of long-range electric vehicles (EVs) and renewable energy harvesting technologies requires superior energy storage devices with higher energy density and power density [1,2]. Unlike batteries, whose energy conversion is controlled by the kinetics of electrochemical reactions, the capacitance of supercapacitors is achieved by interfacial charge transfer, which enables short-term energy storage and burst-mode power delivery [3]. Therefore, supercapacitors can effectively adjust the intermittent energy flow, demonstrating a huge potential for extensive applications such as wearable electronic devices, starting/braking of EVs, and grid energy storage [4–7]. Because of such interface-controlling mechanism, the electrode materials in supercapacitors need to have a large specific surface area to achieve electrochemical high-performance [8]. The 2D morphology renders graphene a high theoretical specific surface area of 2630 m^2/g [9]. Coupling with its outstanding conductivity and mechanical strength, graphene has been widely employed in batteries and supercapacitors [10–13]. Graphene alone can be assembled into superior electrostatic double-layer capacitors (EDLCs), which restore and deliver energy through the Helmholtz double layer at the interface, leading to outstanding power density and lifespan [14–17]. Hybrid supercapacitors with a superior combination of power density and energy density were realized by compositing electrochemical active materials with or doping functional groups onto graphene sheets [18–21]. Up to now, graphene is often derived from nonrenewable resources, such as graphite and fossil fuels via complicated procedures with hazardous chemicals and/or energy-consuming mechanical exfoliation. An alternative carbon source for spuercapacitor electrode materials is biomass. Activated carbon has been fabricated from biomass materials and exhibited competitive properties [22–30]. For instance, flexible and conductive activated cotton textile has been used to construct supercapacitors; [23] activated carbon derived from banana peel has an orderly arranged porous structure, which not only facilitated electrolyte permeation but also promoted the deposition of $NiCo_2O_3$ nanowires [24]. Moreover, carbon materials derived from biomass are usually doped with various electrochemical active functional groups which exhibit pseudocapacitance [29,30]. However, biomass-derived activated carbon often lacks nanostructures and high specific surface area, leading to limited specific capacitance. Can we synthesize nanostructured, graphene-like carbon materials from biomass by feasible and low-cost approaches?

In addition to electrochemical properties, future supercapacitors need to be safe and flexible for wearable electronic devices and car interior structures [31–33]. Solid electrolytes are essential to achieve high safety and flexibility. So far, gel-like solid electrolytes are mainly developed from engineering polymers [34–37]. For instance, a PVA–$LiClO_4$ gel electrolyte exhibited an ionic conductivity of 48 mS/cm and a PPDP/LiCl gel electrolyte enabled a feasible ion migration channel, leading to superior volumetric energy density of the supercapacitors

* Corresponding author.
E-mail address: xl3p@virginia.edu (X. Li).

https://doi.org/10.1016/j.nanoen.2019.104045
Received 11 July 2019; Received in revised form 8 August 2019; Accepted 20 August 2019
Available online 22 August 2019

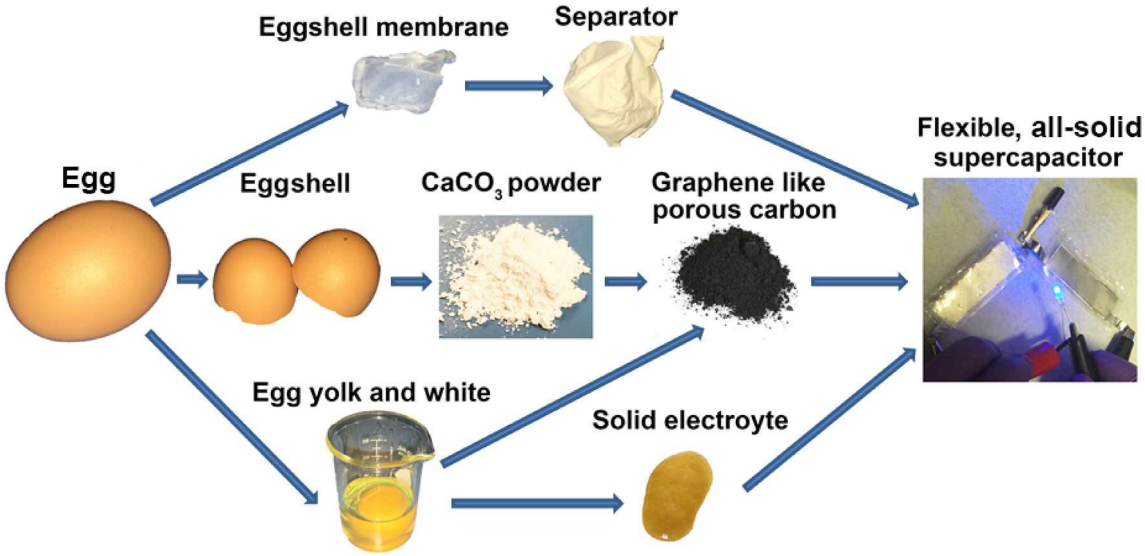

Fig. 1. Schematic illustration of deriving all-solid, flexible supercapacitors from eggs. Eggshell membrane was used as the separator after being rinsed by dilute water and ethanol. Eggshell was calcified at high temperature, forming $CaCO_3$ powders which were used as templates for porous carbon. Egg yolk and egg white were mixed homogeneously. One part of them was mixed with eggshell derived $CaCO_3$ powders and then pyrolyzed, forming graphene-like, egg-derived carbon (EC). Another part of the egg yolk and egg white was treated by KOH to form a gel-like solid electrolyte. Flexible, all-solid supercapacitors were then assembled.

[34,35]. Intriguingly, gel-like polymers and biofilms widely appear in biomass, which are able to store liquid and facilitate ion equilibrium, showing the potential for solid electrolytes [38–40].

Therefore, nature has offered us all essential sources for every component of supercapacitors, ranging from carbonaceous materials for electrodes to macromolecular hydrogels and films for solid electrolytes and separators. However, unlike synthetic materials, biological components often consist of different ingredients with distinct properties. If only one ingredient is used, separating, sorting, disposing, and recycling of the rest will inevitably increase the cost and violate sustainability. Can we achieve comprehensive and effective utilization of biomass in the fabrication of energy storage devices? Here, we report flexible, all-solid supercapacitors from eggs (Fig. 1). Along with the tremendous consumption of eggs is a large amount of inedible eggshell and broken or expired eggs. It is practically significant if these biowastes can be converted to high-value added products. In this study, egg white/yolk and eggshell acted as the carbon source and sacrificial templates for porous activated carbon, respectively. The egg-derived 2D graphene-like carbon sheets with a thickness of 1.25 nm exhibited an outstanding combination of energy density and power density when being used in supercapacitor electrodes due to their high specific surface area (1527.2 m^2/g) and naturally doped functional groups. Egg white/yolk also reacted with KOH, forming gel-like solid electrolyte with competitive ionic conductivity and water preservation. With eggshell membrane as a superb separator, flexible, all-solid supercapacitors were assembled which exhibited superlative electrochemical performance and mechanical flexibility. The proof-of-concept study provides inspirations of comprehensive and effective utilization of biomass materials for energy storage. The eggshell-enabled 2D graphene-like carbon fabrication and protein-derived solid-state electrolytes should find more applications in various fields.

2. Experimental section

2.1. Preparation of eggs

Fresh eggs were cracked in half and the egg white/yolk was separated from the eggshell. The egg white/yolk was stirred vigorously for 1 h to achieve a homogeneous mixing. The eggshell membrane was carefully peeled from the eggshell and rinsed by ethanol and dilute water three times to remove residual egg white.

2.2. Fabrication of egg-derived carbon (EC) and activated egg-derived carbon (AEC)

The eggshell was heat-treated at 500 °C for 1 h to eliminate the organic ingredients. After calcification, the eggshell pieces were grind into white powders. The calcified eggshell powders were stirred with liquid egg white/yolk mix for 2 h with a weight ratio of 1:2. The hybrid slurry was then freeze-dried and pyrolyzed at 550 °C, 650 °C, 750 °C, 850 °C, and 950 °C for 1 h in a tube furnace with the protection of argon. After the high-temperature treatment, the obtained powders were rinsed by 0.1 M HCl and dilute water to eliminate $CaCO_3$ and other impurities. After ultrasonication, graphene-like egg-derived carbon (EC) was fabricated. A two-step KOH treatment was employed to further activate the EC. Specifically, the freeze-dried egg white/yolk with eggshell powders was first heat-treated at 450 °C. The weight of ECs left after 450 °C treatment was calculated by the results of TGA tests. KOH solution and 450 °C treated powders were mixed with a weight ratio between KOH and carbon of 0.3, 1, 2, and 3. The as-obtained suspension was dried at 60 °C for 8 h and further heat-treated at 650 °C after stirred for 10 min. After the activation, the obtained powders were rinsed by 0.1 M HCl and dilute water, forming activated egg-derived carbon (AEC) with porous structures.

2.3. Fabrication of egg-derived, all-solid electrolyte

The egg white/yolk mix was mixed with 6 M KOH solution with a volume ratio of 1:1. Upon mixing, the egg white/yolk reacted with KOH quickly, forming gel-like clusters. The gel-like clusters were unstable. After 2–4 h standing, the clusters gradually dissolved, forming a highly viscous paste. By manipulating the time of drying, the solid-state electrolyte was synthesized.

2.4. Assembling of supercapacitors

The as-fabricated ECs/AECs were mixed with carbon black and PVDF with a weight ratio of 80:10:10. NMP was then infilled into the mixed powders. The formed slurry was homogeneously coated on stainless steel plates and dried at 60 °C for 8 h. For the construction of

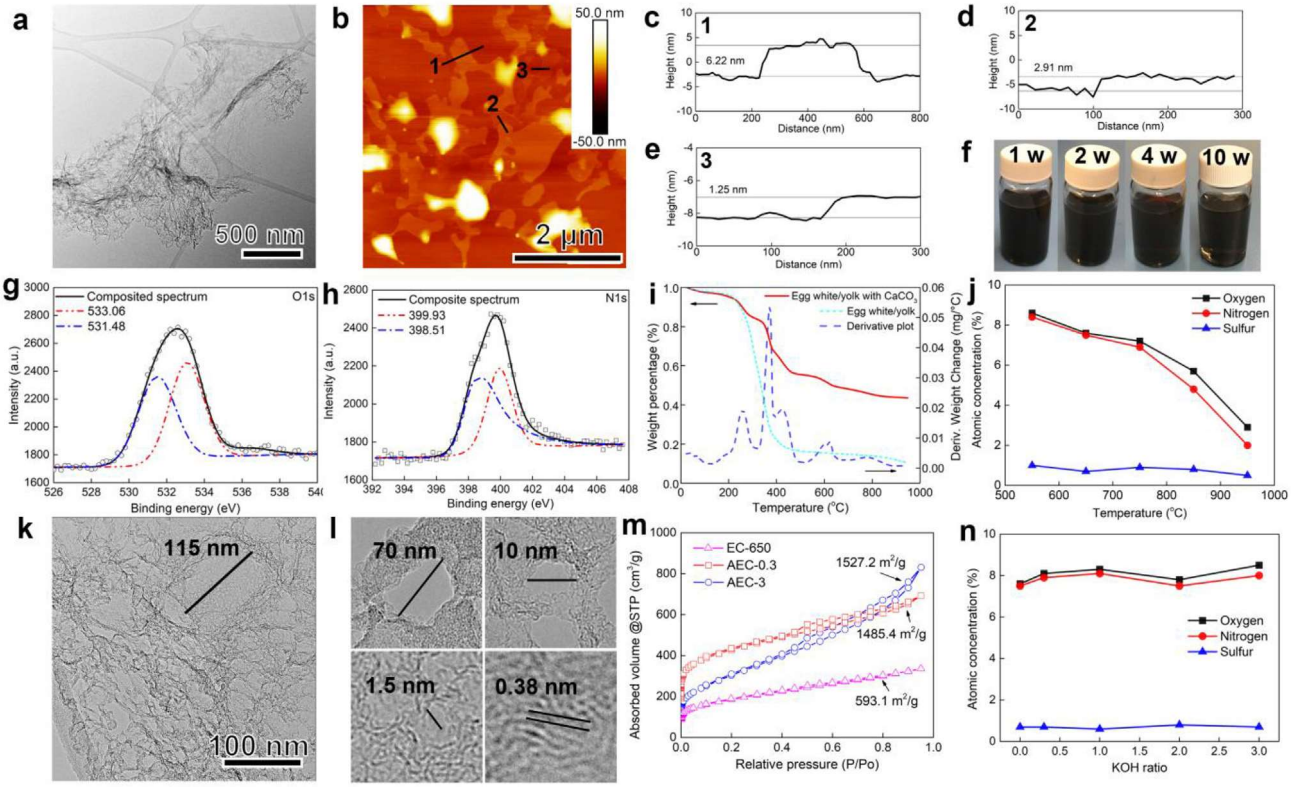

Fig. 2. Graphene-like egg-derived carbon (EC) and activated egg-derived carbon (AEC). **a** TEM inspection of EC derived at 650 °C (EC-650), showing thin and wrinkly morphology. **b** AFM inspection of EC-650. **c-e** Thickness of EC-650 sheets at locations 1, 2, and 3 in the AFM image. **f** EC-650 sheets were dispersed in dilute water, showing no apparent agglomeration after 10 weeks. **g** XPS O 1s spectrum of EC-650. **h** XPS N 1s spectrum of EC-650. **i** TGA tests of pure egg white/yolk and egg white/yolk with eggshell derived $CaCO_3$ powders. **j** Atomic concentration of oxygen, nitrogen, and sulfur of EC derived at different temperatures. **k** TEM inspection of KOH activated EC-650 (AEC). The weight ratio between the EC and KOH was 0.3 (AEC-0.3). **l** Close-up inspection of the nanopores and lattice structure. **m** Nitrogen adsorption and desorption curves of EC-650, AEC-0.3, and AEC-3. **n** Atomic concentration of oxygen, nitrogen, and sulfur of AEC treated by different amount of KOH.

the three-electrode system, a piece of EC/AEC electrode was used as the working electrode, pure Pt plate with the same size was used as the counter electrode, saturated calomel electrode as the reference electrode, and 6 M KOH solution as the electrolyte. For the assembling of symmetric two-electrode supercapacitors, two pieces of commensurate AEC electrodes were used as working electrodes, a piece of filter paper or eggshell membrane was used as the separator, and 6 M KOH solution or egg-derived solid electrolyte was used as the electrolyte. Electrodes, separator, and electrolyte were sealed into 2032 coin cells. For the assembling of all-solid, flexible supercapacitors, the egg-derived solid electrolyte was homogeneously painted on the AEC electrodes and eggshell membrane separators. Stainless steel foils, electrodes, and separator were then sealed together into a flexible plastic cover.

2.5. Materials characterization

The as-prepared ECs/AECs and egg-derived electrolyte were characterized by X-ray diffraction (XRD, a PANalytical X'Pert Pro Multi-Purpose Diffractometer (MPD) equipped with Cu K_α radiation ($\lambda = 0.15406$ nm)), scanning electron microscopy (SEM, FEI Quanta 650 with EDS detector), high resolution transmission electron microscopy (HRTEM, FEI Titan), atomic force microscopy (AFM, Bruker ICON), Raman spectroscopy (a Renishaw inVia Raman microscope at the wavelength of 514 nm), and X-ray photoelectron spectroscopy (XPS, ULVAC-PHI, Inc.). Thermogravimetric analysis (TGA) was performed on a TA Instruments Q50 in an N_2 atmosphere with a heating rate of 5 °C/min to 950 °C. The specific area and pore size of ECs/AECs were measured using a Quantachrome Autosorb iQ nitrogen adsorption-desorption analyzer and calculated by the Brunauer–Emmett–Teller (BET) theory. To measure their zeta potentials, the samples were homogeneously dispersed in DI water. The zeta potential was measured using a Malvern Zetasizer Nano ZS.

2.6. Electrochemical characterization

The electrochemical properties of supercapacitor electrodes were measured with both three-electrode and two-electrode electrochemical systems using a CHI 660E electrochemical workstation. Cyclic voltammetry (CV) was performed at different scan rates. Galvanostatic charge/discharge curves were obtained at different current densities. Electrochemical impedance spectra (EIS) were measured in the frequency range from 100 KHz to 0.1 Hz with an AC perturbation of 5 mV.

3. Results and discussion

3.1. Synthesis and characterization of egg-derived graphene-like carbon

Eggs from grocery stores were cracked and egg white/yolk was separated from eggshell. The eggshell membrane was carefully peeled from the eggshell. A close-up inspection of eggshell under scanning electron microscopy (SEM) revealed a rough surface with micron-sized pores (Figs. S1a and S1b in Supplementary data). The eggshell was heat-treated at 500 °C in an open environment to eliminate residual organic matters, turning it into high-purity $CaCO_3$ powders with a diameter of ~1.5 μm (Figs. S1c and S1d). The egg white and yolk were homogeneously mixed at room temperature and then blended with the eggshell derived $CaCO_3$ powders with a weight ratio of 2:1. After stirring 2 h, a light yellow paste was obtained. The paste was then frozen and lyophilized for 6 h, forming a light-yellow cake. The weight loss of egg white/yolk after freeze-drying was about 75%, suggesting that the

weight ratio between egg white/yolk and $CaCO_3$ powders in the freeze-dried cake was 1:2. The cake was subsequently transferred into a tube furnace and heat treated at different temperatures with the protection of argon for 1 h. The obtained powders were stirred with 0.1 M HCl. After rinsed by dilute water, the final product was fine powders with a dark black color (Fig. 1). Intriguingly, unlike the directly pyrolyzed egg white/yolk which exhibited smooth surface (Fig. S2a), the egg white/yolk carbonized with eggshell-derived $CaCO_3$ powders displayed porous, membrane-like morphology (Fig. S2b). Transmission electron microscopy (TEM) inspection unveiled that the egg carbon derived at 650 °C (EC-650) were thin films with 2D graphene-like morphology and wrinkles (Fig. 2a). Atomic force microscopy (AFM) measurement was carried out to identify the thickness of the EC-650 (Fig. 2b). Most of the EC-650 sheets were thinner than 10 nm while the thinnest part was only about 1.25 nm (Fig. 2c–e), which is close to the thickness of single-layered graphene oxide [41,42]. The Raman spectrum of EC-650 films also exhibited similar features to reduced graphene oxide and activated carbon: stronger D bond peak and obvious 2D bond peak (Fig. S3), indicative of a high degree of defectiveness [43–45]. When being dispersed in dilute water, EC-650 exhibited outstanding dispersing ability that no apparent agglomeration occurred even after 10-week standing (Fig. 2f). The zeta potential of the EC-650 in neutral DI water was measured to be −45 mV, indicative of good stability. Such outstanding dispersing ability and high zeta potential suggested that the EC-650 was naturally doped by functional groups, which can enhance the hydrophilicity of carbon sheets and thereby prevent agglomeration. This hypothesis was verified by energy-dispersive X-ray spectroscopy (EDS) under SEM, in which oxygen and nitrogen were homogeneously dispersed on the EC-650 (Fig. S4). X-ray photoelectron spectroscopy (XPS) tests unveiled that the concentrations of oxygen, nitrogen, and sulfur on EC-650 were 7.6%, 7.5%, and 0.7%, respectively. The 533.06 eV bond and 531.48 eV bond in O 1s spectrum indicative of nitrates and carbonates, respectively (Fig. 2g); the 399.93 eV bond and 398.51 eV bond in N 1s spectrum can be ascribed to N-C bonds and N-H bonds, respectively (Fig. 2f). These functional groups, especially nitrogen-containing functional groups, are expected to introduce pseudocapacitance in the supercapacitors, thereby improving the specific capacitance [29].

A question arises: why the activated carbon synthesized from egg white/yolk with eggshell-derived $CaCO_3$ powders had the 2D graphene-like morphology? A rational assumption is that egg white/yolk wrapped around $CaCO_3$ powders during stirring and carbonized in the following pyrolysis. However, the TEM image of the EC derived at 550 °C (EC-550) displayed a different morphology, a chunk of porous carbon (Fig. S5a). On the contrary, the EC derived at 750 °C (EC-750) exhibited a similar structure to EC-650 (Fig. S5b) while the EC derived at 850 °C (EC-850) had more wrinkles (Fig. S5c). Therefore, the temperature had a notable impact on the final morphology of ECs. Thermogravimetric analysis (TGA) was carried out to reveal the reactions during heating (Fig. 2i). The freeze-dried egg white/yolk displayed a drastic decrease in weight from 300 to 400 °C, indicating that the carbonization of egg white/yolk mainly occurred at 300–400 °C. The weight was stable from 400 °C to 800 °C, where the weight started decreasing again at a slow rate. 15.1% and 10.4% weight remained after 650 °C and 950 °C, respectively. On the contrary, the egg white/yolk with $CaCO_3$ powders sample exhibited staged weight decrease. The corresponding derivative of weight change plot (blue dash line in Fig. 2i) showed a peak at ~250 °C, which can be ascribed to the dehydration of $CaCO_3$ powders. The large peak between 300 and 400 °C was the pyrolysis of egg white/yolk. The peak started at ~500 °C and ended at ~650 °C should contribute to the formation of 2D graphene-like morphology for EC-650 and EC-750 samples. According to the previous studies, this peak is attributed to the decomposition of $CaCO_3$: [46,47].

$$CaCO_3 \rightarrow CaO + CO_2$$

The released gas may blow up the egg white/yolk around the $CaCO_3$ powders, leading to the formation of the 2D morphology. Finally, a small peak appeared at ~800 °C. Since both the carbonization of egg white/yolk and the decomposition of $CaCO_3$ powders had completed, this small peak should be ascribed to another reaction. The atomic percentage values of oxygen, nitrogen, and sulfur derived from XPS of ECs prepared at different temperatures are listed in Fig. 2j. The concentration of oxygen and nitrogen decreased rapidly after 800 °C, indicating that the oxygen- and nitrogen-containing functional groups detached from the ECs, which resulted in the decrease of weight. Such detachment may also introduce voids and defects, leading to the contraction and collapse of carbon sheets, and thereby more wrinkles as shown in EC-850 sheets (Fig. S5c).

The thin film morphology enabled EC-650 a high specific area of 593.1 m^2/g measured by nitrogen adsorption and desorption with Brunauer–Emmett–Teller (BET) theory, [48] which exceeded most of the direct-biomass-derived activated carbon materials that have been reported so far. However, a higher specific surface area with abundant porosity is required for high-performance supercapacitors. KOH treatment was employed to improve the specific surface area of ECs. According to the microstructure (Fig. 2a and Fig. S5), TGA (Fig. 2i), and XPS (Fig. 2j) measurements, the carbonization of egg white/yolk occurred between 300 °C and 400 °C while the thin-film morphology formed after 600 °C. In order to activate ECs without damaging the morphology and surface chemistry, a two-step KOH treatment was carried out (Fig. S6). Specifically, 5 g of freeze-dried egg white/yolk with $CaCO_3$ powders in which egg white/yolk was 1.65 g were heat-treated at 450 °C under the protection of argon. Based on the TGA result (Fig. 2i), the weight of pyrolyzed carbon after 450 °C heat treatment was 17.6% of the freeze-dried egg white/yolk, which was 0.29 g. The as-obtained powders were mixed with 17 mL 1 M, 0.6 M, 0.3 M, and 0.1 M KOH solution, respectively (all solution was dilute from 1 M KOH solution), corresponding to the approximate weight ratio between KOH and pyrolyzed carbon of 3, 2, 1, and 0.3. The KOH treated powders were dried at 60 °C and further activated at 650 °C. Fig. 2k and l are the TEM images of EC-650 carbon films activated by KOH with the weight ratio between KOH and activated carbon of 0.3 (AEC-0.3). A hierarchically porous structure was created on the graphene-like carbon sheets. The pores had the sized ranging from ~1 nm to ~120 nm with walls of multi-layered graphene (Fig. 2l). The KOH treatment almost tripled the specific surface area. When the weight ratio between KOH and EC was 0.3 (AEC-0.3), the BET specific surface area reached 1485.4 m^2/g; when the weight ratio increased to 3 (AEC-3), the specific area exhibited minor improvement to 1572.2 m^2/g. Moreover, the absorption/desorption curve of AEC-3 exhibited a bigger hysteresis loop at intermediate relative pressure, indicative of larger pore size, which was further demonstrated by the pore size distribution derived from Barrett-Joyner-Halenda (BJH) theory [49] (Fig. S7). The majority of nanopores in the AEC-0.3 sample was smaller than 1 nm while the size of nanopores between 1 and 3 nm increased in the AEC-3 sample. The tendency was also validated by TEM inspections of AEC-1 (Fig. S8a) and AEC-3 samples (Fig. S8b), which exhibited a larger pore size than AEC-0.3 (Fig. 2k and i). A critical question is whether the KOH treatment changed the surface chemistry of ECs. Atomic concentrations of nitrogen, oxygen, and sulfur derived from XPS spectra of samples treated by different amount of KOH were demonstrated in Fig. 2n. Unlike the temperature of heat treatments (Fig. 2j), the amount of KOH had almost no influence on the surface chemistry of egg-derived carbon samples. This may be because the conversion from egg white/yolk to activated carbon mainly occurred between 300 and 400 °C (Fig. 2i) while the powders were treated at 450 °C before being mixed with KOH, leading to minor influence of KOH treatment on the surface chemistry.

3.2. Electrochemical performance of egg-derived carbon in supercapacitors

To measure the electrochemical properties of the graphene-like carbon derived from eggs, ECs/AECs were mixed with carbon black and

polyvinylidene fluoride (PVDF) in a ratio of 80:10:10. The mix was dispersed in N-Methyl-2-Pyrrolidone (NMP) and the slurry was homogeneously coated on a stainless steel plate. The electrodes were baked at 60 °C for 8 h and then cut into pieces with desired shapes. Three-electrode system with Pt as the counter electrode, saturated calomel electrode as the reference electrode, and 6 M KOH as the electrolyte was set up. The cyclic voltammetry (CV) curves of the ECs derived at different temperatures are shown in Fig. S9a. The electrochemical performance of EC-650 electrode had a notable improvement compared with EC-550 electrode due to the formation of graphene-like morphology. The CV curve of EC-650 exhibited a morphology which deviated from quasi-rectangle, the typical shape of EDLCs. Such deviation without notable anodic or cathodic peaks is often ascribed to fast, reversible, successive surface redox reactions and/or insufficient conductivity of the active materials [50]. It is likely that the functional groups which were found on ECs (Fig. 2g and h) delivered pseudocapacitance during charging/discharging. The CV curves of EC-750 and EC-850 showed less deviation from quasi-rectangle, indicative of the detachment of functional groups and improvement of conductivity due to higher-temperature pyrolysis. Under the current conditions, EC-650 exhibited the highest specific capacitance in terms of the area covered by the CV curve. The specific capacitance of EC-650 electrode is comparable with reduced graphene oxide (rGO) derived electrode (Fig. 3a). KOH activation largely improved the electrochemical performance of egg-derived carbon. The area covered by the CV curves of AECs was much larger than that of EC-650 and rGO (Fig. 3a). The CV curve of AEC-0.3 electrode exhibited slightly better performance than AEC-1 and AEC-3 electrodes (Fig. 3a). The tendency that carbon materials treated by higher concentrations of KOH exhibited lower specific capacitance reported in previous studies [29]. Fig. 3b shows the CV curves of the AEC-0.3 electrode tested at different scan rates. With the increase of scan rate, the CV curves showed larger tilt due to the polarization. The specific capacitance values were calculated from galvanostatic charge/discharge curves (Fig. 3c) by equation (1):

$$C = \frac{\int i\,dt}{\Delta V * m} \tag{1}$$

where i is the current, t is the discharge time, ΔV is the potential difference, and m is the weight of the active materials. The specific capacitance of AEC-0.3 derived electrode delivered a specific capacitance of 420.8 F/g at 0.5 A/g. The specific capacitance decreased to 265.1 F/g when the current density increased to 10 A/g, corresponding to a capacitance retention rate of 63%.

Since the three-electrode system focuses on electrochemical properties of a single electrode and cannot reflect the real-life performance of an energy storage application, symmetric supercapacitors were assembled to examine the practical utilization of the AEC-based supercapacitors. Specifically, two pieces AEC-0.3 electrodes with the same

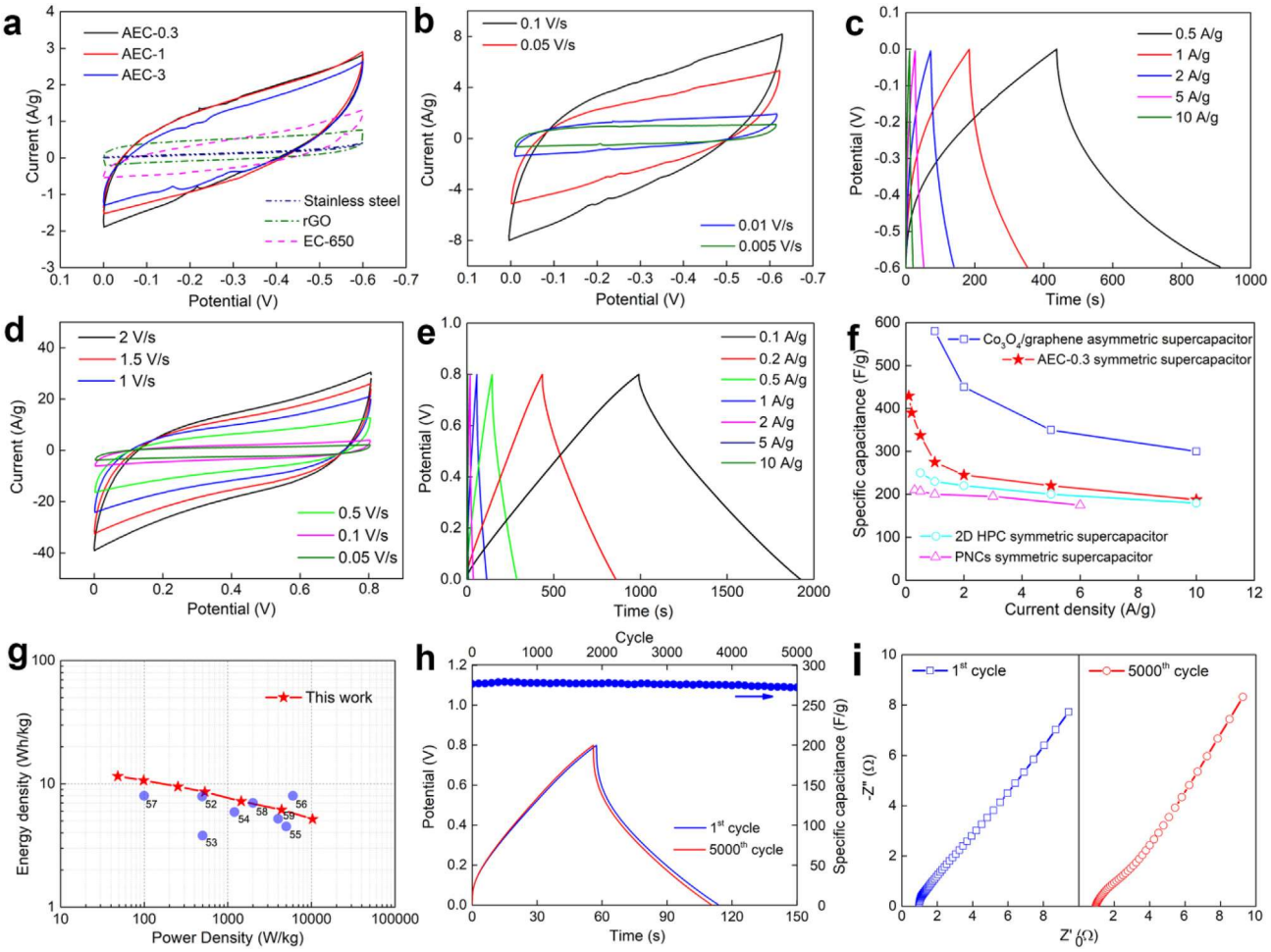

Fig. 3. Electrochemical performance of electrodes derived from ECs and AECs. **a** CV curves of AECs, EC-650, and rGO electrodes in the three-electrode system scanned at 0.01 V/s. **b** CV curves at different scan rates of the electrode derived from AEC-0.3 in the three-electrode system. **c** Galvanostatic charge/discharge curves at different current densities of the AEC-0.3 electrode. **d** CV curves at different scan rates of the symmetric supercapacitor derived from AEC-0.3 electrodes. **e** Galvanostatic charge/discharge curves of the symmetric supercapacitor. **f** Comparative specific capacitance of the symmetric supercapacitors derived from AEC-0.3 and other supercapacitors. **g** Ragone plots of the as-assembled symmetric supercapacitor derived from AEC-0.3. **h** Cyclic performance of the symmetric supercapacitor derived from AEC-0.3. **i** EIS of the symmetric supercapacitor before cycling and after 5000 cycles.

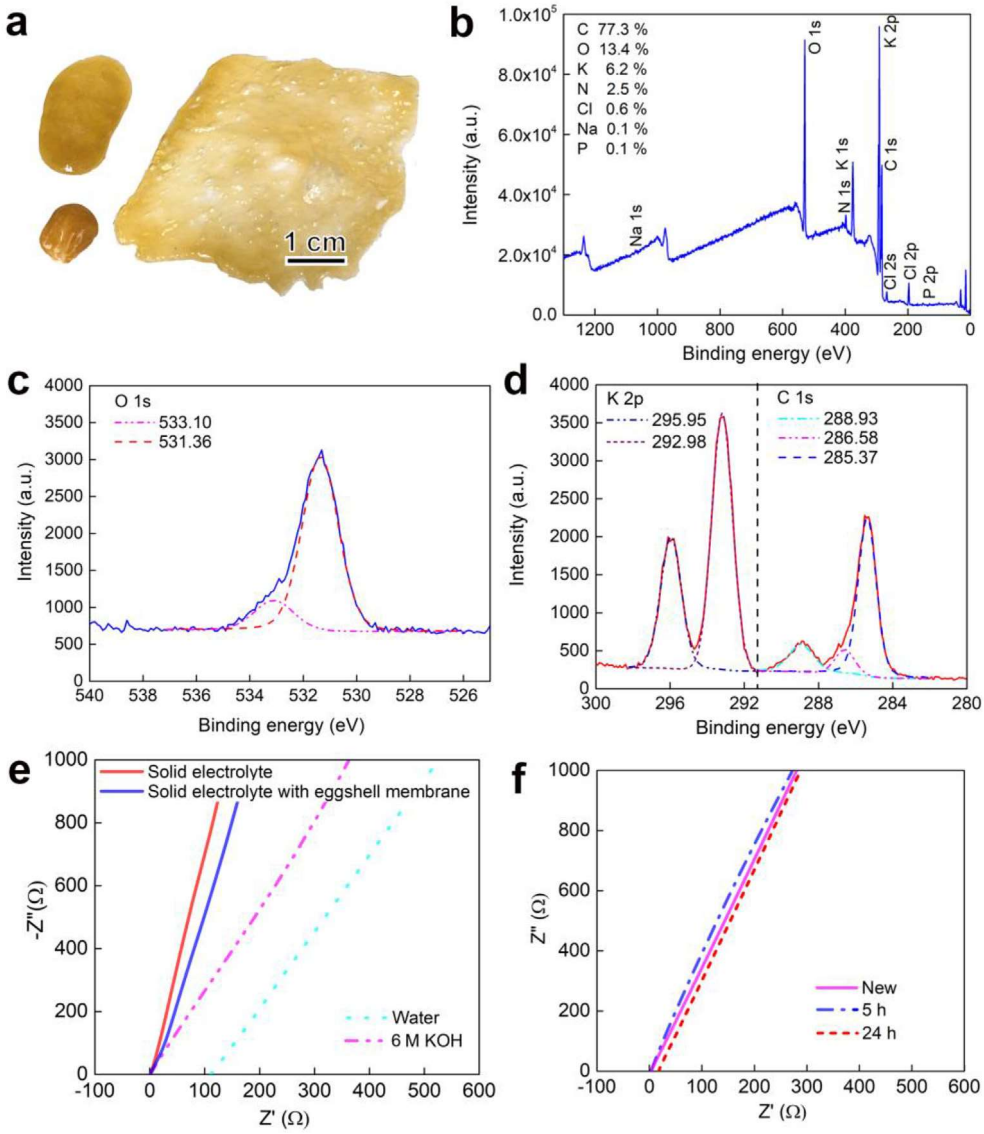

Fig. 4. Solid-state electrolyte derived from egg white/yolk. **a** Photograph of the solid-state electrolyte. **b** Comprehensive XPS spectrum of the solid-state electrolyte. **c** XPS O 1s spectrum. **d** XPS C 1s and K 2p spectra. **e** EIS spectra of water with filter paper, 6 M KOH solution-saturated filter paper, egg-derived solid electrolyte, and egg-derived solid electrolyte with eggshell membrane. **f** EIS spectra of egg-derived solid electrolyte with eggshell membrane and after 0 h, 5 h, and 24 h in open air.

size were assembled with a 6 M KOH solution-saturated filter paper as the separator into a 2032 coin cell. The CV curves exhibited quasi-rectangular shapes with excellent stability even at a high scan rate (Fig. 3d). No anodic and cathodic peaks were observed in the CV curve scanned at 0.01 V/s (Fig. S9b). The galvanostatic charge/discharge curves displayed triangular shapes (Fig. 3e). The specific capacitances of single electrodes at different current density were calculated by the equation:

$$C = \frac{4 * i * \Delta t}{\Delta V * m} \quad (2)$$

where m is the total weight of active materials in both electrodes. At low current density regime, the specific capacitance was comparable to supercapacitors derived from metal oxides (Fig. 3f) [18,51]. The specific capacitance decreased with the increase of current density. At high current density regime, the specific capacitance of AEC-0.3 derived symmetric supercapacitor was close to other supercapacitors derived from 2D carbon materials with a similar specific surface area [29,52]. A rational explanation is that the pseudocapacitance from functional groups mainly enhanced the specific capacitance of the symmetric supercapacitor at the low current density regime while electron double layer capacitance mainly contributed to the specific capacitance at the high current density regime. The energy density and power density of symmetric supercapacitor system were calculated by the following equations:

$$E = \frac{1}{8} C \Delta V^2 \quad (3)$$

$$P = \frac{E}{\Delta t} \quad (4)$$

where C is the specific capacitance of a single electrode, ΔV refers to the potential change within the discharge time Δt. Ragone plots of the as-assembled symmetric supercapacitor derived from AEC-0.3 showed an excellent combination of power density and energy density (Fig. 3g). At low current density regime, the symmetric supercapacitor exhibited an energy density outperformed most of the graphene or carbon-based symmetric supercapacitors [53–60], indicating that the high specific surface and naturally grafted functional groups mutually promoted, making 2DGC-derived supercapacitors single-phase hybrid supercapacitors. The as-assembled symmetric supercapacitor exhibited

almost no capacitance decay after 5000 cycles at a current density of 1 A/g (Fig. 3h). Electrochemical impedance spectroscopy (EIS) was then used to validate the changes of internal impendence of the supercapacitor before and after cycling (Fig. 3i). The intercept between the EIS curve and the Z′ axis is the equivalent series resistance (R_Ω), which stems from the electrolyte resistance, the intrinsic resistance of the active material, and the interfacial contact resistance between electrodes and current collectors. The semicircle in the intermediate frequency regime indicates the impedance of the charge transfer between the electrodes and electrolyte (R_{ct}), which is mainly influenced by the ion/electron transfer on the surface of the electrodes. After 5000 cycles, R_Ω remained the same, about 1 Ω, while the R_{ct} increased. The self-discharging test was carried out to reveal the chronic stability of the symmetric supercapacitor. The potential of the symmetric supercapacitor decayed to 50% (0.4 V) after 1290 s; 0.22 V remained after 10000 s (Fig. S8c). Therefore, although the functional groups provided pseudocapacitance to the supercapacitor, they also accelerated the self-discharging rate.

3.3. Synthesis of egg white/yolk-derived solid electrolyte

In addition to electrode materials, solid electrolytes also can be fabricated from eggs. When mixing 6 M KOH with egg white, a hydrogel formed as shown in Fig. S10a. This hydrogel was not stable and decomposed to liquid after several hours. When mixing 6 M KOH with egg yolk, a viscous suspension formed (Fig. S10b). The yellow suspension could not sustain the shape and would dry within several hours. In order to utilize their advantages and overcome the drawbacks, as well as to simplify the fabrication procedures, 6 M KOH solution was homogeneously stirred with liquid egg white/yolk with a volumetric ratio of 1:1. After drying the mix at room temperature for 24 h, the formed paste was highly viscous. The gel-like paste can sustain the shape and be spread into thin films (Fig. 4a). The thin film can reserve moist in an open environment for hours. The comprehensive XPS scanning unveiled that the dried egg-derived electrolyte contains elements including C, O, K, N, and minor Cl, Na, P (Fig. 4b). EDS elements analysis further validated the results (Fig. S11). XRD spectrum revealed that the egg-derived electrolyte contained KOH, KCL, and K_2CO_3 (Fig. S12). The XPS O 1s spectrum (Fig. 4c) exhibited peaks at the binding energy of 533.10 eV and 531.36 eV, indicative of the existence of –OH bonds and –CO bonds. The K 2p spectrum showed two distinctive peaks at 295.95 eV and 292.98 eV, indicating that the K-O bonds and K-H bonds formed (Fig. 4d). The C 1s peak can be divided into three peaks located at 288.93 eV, 286.58 eV, and 285.37 eV, corresponding to C-O, C-Cl, and C-P bonds (Fig. 4d). After baked at 80 °C for 24 h, the weight of the egg-derived gel-like paste reduced by 72%, indicative of over 70% water content, which is close to that of pure egg white/yolk.

Eggshell membrane was then employed as the separator. The eggshell membranes were carefully peeled from eggshells and rinsed by water and ethanol to remove residual egg white and egg yolk. As shown in Fig. S13, the eggshell membrane displayed interlaced fibers ranging in diameter from 0.5 to 1 μm, which constructed an interwoven, macroporous network with a thickness of about 50 μm. Such interleaved fibular structure is expected to be able to facilitate ion transfer and maintain mechanical robustness. Previous studies have demonstrated that eggshell membrane can be a qualified separator for energy storage devices [39,40]. The eggshell membrane derived separators starts decomposition at over 200 °C and has a tensile strength of 6.59 MPa, indicating competitive thermal and mechanical stability. The egg white/yolk derived solid electrolyte was then coated on the eggshell membranes, showing no noticeable degradation, indicating that they are mutually compatible.

A critical question is: what is the ionic conductivity of the egg-derived, all-solid-state electrolyte with eggshell membrane separator? Fig. 4e lists the comparative EIS plots of dilute water with filter paper, 6 M KOH solution with filter paper, egg white/yolk derived solid electrolyte, and egg white/yolk derived solid electrolyte with the eggshell membrane separator. All the plots exhibited similar single-line morphology at intermediate and low-frequency regimes (Warburg impendence) without semicircles at high-frequency regime (charge transfer impendence), indicative of diffusion-controlled processes [61]. The slopes of the Warburg lines were affected by the finite-thickness effects of electrolytes. The ionic conductivity σ can be calculated via equation (5): [62,63].

$$\sigma = \frac{d}{A * R_e} \tag{5}$$

where d is the thickness of electrolyte, A is the contact area, and R_e is the resistance of the electrolyte. The resistance of the electrolyte can be derived from the intercept of Z′ axis and the straight line obtained by the linear regression of the EIS plot in the high-frequency regime. Apparently, dilute water had a much larger resistance than the other electrolytes. If we consider the thickness of 6 M KOH electrolyte is equal to the thickness of filter paper and the thickness of egg white/yolk derived solid electrolyte is equal to that of the eggshell membrane, the ionic conductivity of 6 M KOH-saturated filter paper was calculated to be 26.9 mS/cm. The ionic conductivity of solid electrolyte derived from egg white/yolk was 9.3 mS/cm. When the eggshell membrane was used as the separator, the ionic conductivity decreased to 3.8 mS/cm. Therefore, the egg white/yolk-derived solid electrolyte exhibited an ionic conductivity comparable with other hydrogels from engineering polymers [34–37]. Worth mentioning is that the ionic conductivity of the egg-derived electrolyte/eggshell membrane hybrid exhibited no notable degradation even after 24 h in an open environment (Fig. 4f), indicative of outstanding moist preservation ability. The egg-derived, all-solid-state electrolyte thin film dried out at room temperature in about 40 h.

3.4. Electrochemical performance of whole egg-derived all-solid supercapacitor

Excitingly, all-solid, flexible supercapacitors were successfully assembled by the AEC-based electrode, egg white/yolk-derived solid electrolyte, and eggshell membrane separator (Fig. 5a). The solid electrolyte provided the supercapacitors outstanding flexibility. As shown in Fig. 5b, the CV curves of the flexible, all-solid supercapacitor had no distortion in flat, bend, and twist conditions. Similarly, the specific capacitance remained unchanged when bending or twisting the supercapacitor (Fig. 5c). When connecting two all-solid supercapacitors in series, the supercapacitor pack enlightened a LED for hundreds of seconds (Fig. 5d), implying a potential for practical applications. 2032 coin cells were used to identify the electrochemical performance of symmetric supercapacitors assembled with AEC-0.3 electrodes and egg-derived solid electrolyte (Fig. S14). Comparing with the supercapacitors used the liquid electrolyte, the galvanostatic charge/discharge curves of the all-solid supercapacitor exhibited IR drop at the early stage of discharge, especially at high current density regime (Fig. S14a). The IR drop may be because of the relatively low ionic conductivity of egg white/yolk derived all-solid electrolyte, which also deteriorated the rate ability. At low current density regime, the specific capacitance of the all-solid supercapacitor was comparable with that of the liquid supercapacitors (Fig. S14b). The all-solid supercapacitor had a capacitance retention rate of 80% after 5000 cycles at the current density of 1 A/g (Fig. S14c). Comparing with the results of symmetric supercapacitors constructed with liquid electrolyte (Fig. 3h), the decay of the specific capacitance was mainly ascribed to the degradation of the solid electrolyte. After 5000 cycles, the equivalent series resistance (R_Ω) and charge transfer resistance (R_{ct}) both decreased due to the closer contact between active materials and electrolyte (Fig. S14d). However, the ion conductivity of the solid electrolyte reduced from 3.8 mS/cm to 2.1 mS/cm.

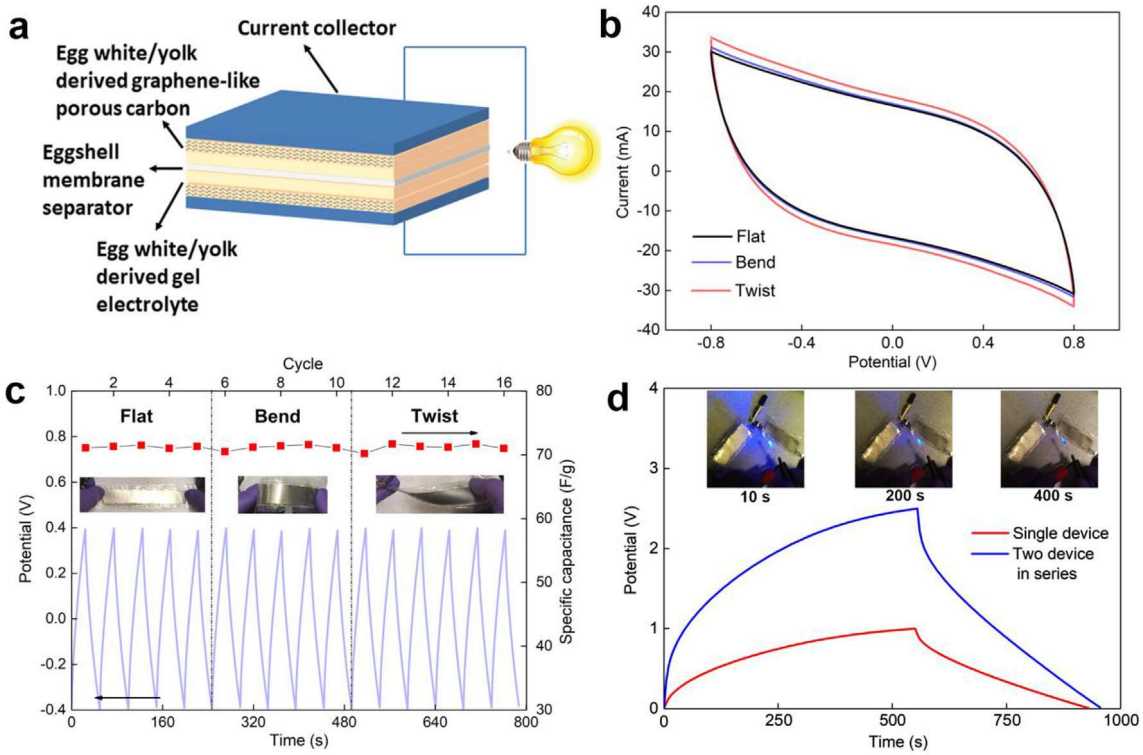

Fig. 5. All-solid, flexible symmetric supercapacitors assembled by AEC-0.3 electrodes, egg-derived solid electrolyte, and eggshell membrane separator. **a** Schematic illustration of the as-assembled all-solid supercapacitor. **b** CV curves of the all-solid, flexible supercapacitor in flat, bend, and twist conditions. **c** Cyclic charge/discharge curves of the all-solid, flexible supercapacitor in flat, bend, and twist conditions. **d** Two egg-derived, all-solid supercapacitors in series enlightened LEDs.

4. Conclusion

In summary, individual components of an egg were used to construct all-solid, flexible supercapacitors. The eggshell was calcified, forming high-purity $CaCO_3$ powders. Egg white/yolk was homogeneously mixed with the eggshell-derived $CaCO_3$ powders. After freeze-drying and pyrolysis, graphene-like egg-derived carbon (EC) sheets were synthesized with the thinnest thickness of only 1.25 nm. After KOH activation, the specific surface area of activated egg-derived carbon (AEC) was further increased to 1572.2 m^2/g. The hierarchically porous structure and the naturally grafted functional groups rendered the supercapacitors derived from AECs a high specific capacitance and an outstanding combination of energy density and power density. KOH treated egg white/yolk mix served as the solid-state electrolyte with competitive ionic conductivity (9.3 mS/cm). Eggshell membrane was found to be an excellent natural separator. As a result, a whole egg-derived, all-solid, flexible supercapacitor was developed with superlative performance. The prototypical study opens up a new opportunity for comprehensively utilizing biomass materials for energy storage. The eggshell-enabled graphene-like carbon and protein-derived solid electrolyte are expected to find more applications in extensive fields.

Author contributions

Y.Z. and X.L. conceived the idea. Y.Z. and J.H. carried out the materials synthesis and supercapacitor assembly. Y.Z. carried out electrochemical tests and microstructural characterization. Y.Z. and X.L. co-wrote the paper. Z.G. and J.H. discussed and commented on the paper.

Acknowledgements

Financial support for this study was provided by the U.S. National Science Foundation (CMMI-1728042). The authors thank the staff members at the University of Virginia NMCF for electron microscopy technical support.

Appendix A. Supplementary data

Supplementary data to this article can be found online at https://doi.org/10.1016/j.nanoen.2019.104045.

References

[1] S. Chu, Y. Cui, N. Liu, The path towards sustainable energy, Nat. Mater. 16 (2017) 16–22.
[2] E. Karden, S. Ploumen, B. Fricke, T. Miller, K. Snyder, Energy storage devices for future hybrid electric vehicles, J. Power Sources 168 (2007) 2–11.
[3] P. Simon, Y. Gogotsi, B. Dunn, Where do batteries end and supercapacitors begin? Science 343 (2014) 1210–1211.
[4] T. Ma, H. Yang, L. Lu, Development of hybrid battery – supercapacitor energy storage for remote area renewable energy systems, Appl. Energy 153 (2015) 56–62.
[5] P. Thounthong, V. Chunkag, P. Sethakul, S. Sikkabut, S. Pierfederici, B. Davat, Energy management of fuel cell/solar cell/supercapacitor hybrid power source, J. Power Sources 196 (2011) 313–324.
[6] Z. Zhang, X. Zhang, W. Chen, Y. Rasim, W. Salman, H. Pan, et al., A high-efficiency energy regenerative shock absorber using supercapacitors for renewable energy applications in range extended electric vehicle, Appl. Energy 178 (2016) 177–188.
[7] E. Faggioli, P. Rena, V. Danel, X. Andrieu, R. Mallant, H. Kahlen, Supercapacitors for the energy management of electric vehicles, J. Power Sources 84 (1999) 261–269.
[8] L.L. Zhang, X.S. Zhao, Carbon-based materials as supercapacitor electrodes, Chem. Soc. Rev. 38 (2009) 2520–2531.
[9] F. Bonaccorso, L. Colombo, G. Yu, M. Stoller, V. Tozzini, A.C. Ferrari, et al., Graphene, related two-dimensional crystals, and hybrid systems for energy conversion and storage, Science 347 (2015) 1246501.
[10] G. Wang, L. Zhang, J. Zhang, A review of electrode materials for electrochemical supercapacitors, Chem. Soc. Rev. 41 (2012) 797–828.
[11] A. Ghosg, Y. Lee, Carbon-based electrochemical capacitors, ChemsucChem 5 (2012) 480–499.
[12] Y. Zhang, Z. Gao, N. Song, J. He, X. Li, Graphene and its derivatives in lithium–sulfur batteries, Mater. Today Energy 9 (2018) 319–335.
[13] M.F. El-Kady, Y. Shao, R.B. Kaner, Graphene for batteries, supercapacitors and beyond, Nat. Rev. Mater. 1 (2016) 16033.
[14] M.D. Stoller, S. Park, Y. Zhu, J. An, R.S. Ruoff, Graphene-based ultracapacitors, Nano Lett. 8 (2008) 3498–3502.
[15] Y. Wang, Z. Shi, Y. Huang, Y. Ma, C. Wang, M. Chen, et al., Supercapacitor devices

based on graphene materials, J. Phys. Chem. C 113 (2009) 13103–13107.
[16] C. Liu, Z. Yu, D. Neff, A. Zhamu, B.Z. Jang, Graphene-based supercapacitor with an ultrahigh energy density, Nano Lett. 10 (2010) 4863–4868.
[17] J. Zhao, Y. Jiang, H. Fan, M. Liu, O. Zhuo, X. Wang, et al., Porous 3D few-layer graphene-like carbon for ultrahigh-power supercapacitors with well-defined structure – performance relationship, Adv. Mater. 3 (2017) 1604569.
[18] Q. Liao, N. Li, S. Jin, G. Yang, C. Wang, All-solid-state symmetric supercapacitor based on Co_3O_4 nanoparticles on vertically aligned graphene, ACS Nano 9 (2015) 5310–5317.
[19] X. Cao, B. Zheng, W. Shi, J. Yang, Z. Fan, Z. Luo, et al., Reduced graphene oxide-wrapped MoO_3 composites prepared by using metal-organic frameworks as precursor for all-solid-state flexible supercapacitors, Adv. Mater. 27 (2015) 4695–4701.
[20] W. Zhang, C. Xu, C. Ma, G. Li, Y. Wang, K. Zhang, et al., Nitrogen-superdoped 3D graphene networks for high-performance supercapacitors, Adv. Mater. 9 (2017) 1701677.
[21] Z.Y. Sui, Y.N. Meng, P.W. Xiao, Z.Q. Zhao, Z.X. Wei, B.H. Han, Nitrogen-doped graphene aerogels as efficient supercapacitor electrodes and gas adsorbents, ACS Appl. Mater. Inter. 7 (2015) 1431–1438.
[22] Z. Gao, Y. Zhang, N. Song, X. Li, Biomass-derived renewable carbon materials for electrochemical energy storage, Mater. Res. Lett. 5 (2017) 69–88.
[23] Z. Gao, N. Song, Y. Zhang, X. Li, Cotton textile enabled, all-solid-state flexible supercapacitors, RSC Adv. 5 (2015) 15438–15447.
[24] Y. Zhang, Z. Gao, N. Song, X. Li, High-performance supercapacitors and batteries derived from activated banana-peel with porous structures, Electrochim. Acta 222 (2016) 1257–1266.
[25] R. Tholkappiyan, A.N. Naveen, K. Vishista, Novel eggshell membrane template assisted synthesis of Mn_2O_3 electrode material for supercapacitor applications, AIP Conf. Proc. 1665 (2015) 140011.
[26] B. Li, F. Dai, Q. Xiao, L. Yang, J. Shen, C. Zhang, M. Cai, Activated carbon from biomass transfer for high-energy density lithium-ion supercapacitors, Adv. Energy Mater. 6 (2016) 1600802.
[27] J. Li, S. Ma, L. Cheng, Q. Wu, Egg yolk-derived three-dimensional porous carbon for stable electrochemical supercapacitors, Mater. Lett. 139 (2015) 429.
[28] Z. Li, L. Zhang, B.S. Amirkhiz, X. Tan, Z. Xu, H. Wang, B.C. Olsen, C.M. Holt, D. Mitlin, Carbonized chicken eggshell membranes with 3D architectures as high-performance electrode materials for supercapacitors, Adv. Energy Mater. 2 (2012) 431.
[29] Z. Li, Z. Xu, H. Wang, J. Ding, B. Zahiri, C.M. Holt, et al., Colossal pseudocapacitance in a high functionality–high surface area carbon anode doubles the energy of an asymmetric supercapacitor, Energy Environ. Sci. 7 (2014) 1708.
[30] L. Chen, Y. Zhang, C. Lin, W. Yang, Y. Meng, Y. Guo, et al., Hierarchically porous nitrogen-rich carbon derived from wheat straw as an ultra-high-rate anode for lithium ion batteries, J. Mater. Chem. A 2 (2014) 9684.
[31] L. Liu, Y. Yu, C. Yan, K. Li, Z. Zheng, Wearable energy-dense and power-dense supercapacitor yarns enabled by scalable graphene–metallic textile composite electrodes, Nat. Commun. 6 (2015) 7260.
[32] I. Shown, A. Ganguly, L.C. Chen, K.H. Chen, Conducting polymer-based flexible supercapacitor, Energy Sci. Eng. 3 (2015) 2–26.
[33] W. Liu, M.S. Song, B. Kong, Y. Cui, Flexible and stretchable energy storage: recent advances and future perspectives, Adv. Mater. 29 (2017) 1603436.
[34] X. Peng, H. Liu, Q. Yin, J. Wu, P. Chen, G. Zhang, et al., A zwitterionic gel electrolyte for efficient solid-state supercapacitors, Nat. Commun. 7 (2016) 11782.
[35] N.R. Chodankar, D.P. Dubal, A.C. Lokhande, C.D. Lokhande, Ionically conducting PVA–LiClO4 gel electrolyte for high performance flexible solid state supercapacitors, J. Colloid Interf. Sci. 460 (2015) 370–376.
[36] W.G. Moon, G.P. Kim, M. Lee, H.D. Song, J. Yi, A biodegradable gel electrolyte for use in high-performance flexible supercapacitors, ACS Appl. Mater. Inter. 7 (2015) 3503–3511.
[37] G.K. Veerasubramani, K. Krishnamoorthy, P. Pazhamalai, S.J. Kim, Enhanced electrochemical performances of graphene based solid-state flexible cable type supercapacitor using redox mediated polymer gel electrolyte, Carbon 105 (2016) 638–648.
[38] M. Zhang, L. Song, H. Jiang, S. Li, Y. Shao, J. Yang, J. Li, Biomass based hydrogel as an adsorbent for the fast removal of heavy metal ions from aqueous solutions, J. Mater. Chem. A 5 (2017) 3434.
[39] H. Yu, Q. Tang, J. Wu, Y. Lin, L. Fan, M. Huang, et al., Using eggshell membrane as a separator in supercapacitor, J. Power Sources 206 (2012) 463.
[40] N.S.M. Nor, M. Deraman, R. Omar, E. Taer, R. Awitdrus, Farma, N.H. Basri, B.N.M. Dolah, Nanoporous separators for supercapacitor using activated carbon monolith electrode from oil palm empty fruit bunches, AIP Conf. Proc. 1586 (2014) 68.
[41] Y. Zhang, N. Song, J. He, R. Chen, X. Li, Lithiation-aided conversion of end-of-life lithium-ion battery anodes to high-quality graphene and graphene oxide, Nano Lett. 19 (2018) 512–519.
[42] W. Gao, Graphene Oxide: Reduction Recipes, Spectroscopy, and Applications, Springer, Berlin, Germany, 2015.
[43] D. Yang, A. Velamakanni, G. Bozoklu, S. Park, M. Stoller, R.D. Piner, S. Stankovich, I. Jung, D.A. Field, C.A. Ventrice Jr., R.S. Ruoff, Chemical analysis of graphene oxide films after heat and chemical treatments by X-ray photoelectron and Micro-Raman spectroscopy, Carbon 47 (2009) 145–152.
[44] A. Cuesta, P. Dhamelincourt, J. Laureyns, A. Martinez-Alonso, J.D. Tascón, Raman microprobe studies on carbon materials, Carbon 32 (1994) 1523.
[45] N. Shimodaira, A. Masui, Raman spectroscopic investigations of activated carbon materials, J.Appl. Phys. 92 (2002) 902.
[46] M. Mohamed, S. Yusup, S. Maitra, Decomposition study of calcium carbonate in cockle shell, J. Eng. Sci. Technol. 7 (2012) 1.
[47] T. Witoon, Characterization of calcium oxide derived from waste eggshell and its application as CO_2 sorbent, Ceram. Int. 37 (2011) 3291.
[48] S. Brunauer, P.H. Emmett, E. Teller, Adsorption of gases in multimolecular layers, J. Am. Chem. Soc. 60 (1938) 309.
[49] J.C. Groen, L.A. Peffer, J. Pérez-Ramírez, Pore size determination in modified micro-and mesoporous materials. Pitfalls and limitations in gas adsorption data analysis, Micropor. Mesopor. Mat. 60 (2003) 1.
[50] P. Simon, Y. Gogotsi, Materials for electrochemical capacitors, Nat. Mater. 7 (2008) 845–854.
[51] Q.Y. Liao, S.Y. Li, H. Cui, C. Wang, Vertically-aligned graphene@Mn_3O_4 nanosheets for a high-performance flexible all-solid-state symmetric supercapacitor, J. Mater. Chem. A 4 (2016) 8830.
[52] Y. Li, G. Wang, T. Wei, Z. Fan, P. Yan, Nitrogen and sulfur co-doped porous carbon nanosheets derived from willow catkin for supercapacitors, Nano Energy 19 (2016) 165.
[53] F. Ma, D. Ma, G. Wu, W. Geng, J. Shao, S. Song, et al., Construction of 3D nanostructure hierarchical porous graphitic carbons by charge-induced self-assembly and nanocrystal-assisted catalytic graphitization for supercapacitors, Chem. Commun. 52 (2016) 6673.
[54] Z. Li, D. Wu, Y. Liang, R. Fu, K. Matyjaszewski, Synthesis of well-defined microporous carbons by molecular-scale templating with polyhedral oligomeric silsesquioxane moieties, J. Am. Chem. Soc. 136 (2014) 4805.
[55] Y. Cheng, L. Huang, X. Xiao, B. Yao, L. Yuan, T. Li, et al., Flexible and cross-linked N-doped carbon nanofiber network for high performance freestanding supercapacitor electrode, Nano Energy 15 (2015) 66.
[56] Y.J. Kang, H. Chung, C.H. Han, W. Kim, All-solid-state flexible supercapacitors based on papers coated with carbon nanotubes and ionic-liquid-based gel electrolytes, Nanotechnology 23 (2012) 065401.
[57] Y. Xu, Z. Lin, X. Huang, Y. Liu, Y. Huang, X. Duan, Flexible solid-state supercapacitors based on three-dimensional graphene hydrogel films, ACS Nano 7 (2013) 4042.
[58] E. Raymundo-Piñero, F. Leroux, F. Béguin, A high-performance carbon for supercapacitors obtained by carbonization of a seaweed biopolymer, Adv. Mater. 18 (2006) 1877.
[59] Y. Tao, X. Xie, W. Lv, D.M. Tang, D. Kong, Z. Huang, et al., Towards ultrahigh volumetric capacitance: graphene derived highly dense but porous carbons for supercapacitors, Sci. Rep. 3 (2013) 2975.
[60] B.G. Choi, M. Yang, W.H. Hong, J.W. Choi, Y.S. Huh, 3D macroporous graphene frameworks for supercapacitors with high energy and power densities, ACS Nano 6 (2012) 4020.
[61] C. Ho, I.D. Raistrick, R.A. Huggins, Application of A-C techniques to the study of lithium diffusion in tungsten trioxide thin films, J. Electrochem. Soc. 127 (1980) 343.
[62] R.A. Huggins, Simple method to determine electronic and ionic components of the conductivity in mixed conductors a review, Ionics 8 (2002) 300.
[63] B. Huber, L. Rossrucker, J. Sundermeyer, B. Roling, Ion transport properties of ionic liquid-based polyelectrolytes, Solid State Ion. 15 (2013) 247–248.